The Astrophysical Journal, 1001:181 (15pp), 2026 April 20 https://doi.org/10.3847/1538-4357/ae5243

SN 2023taz: Implications for the UV Diversity of Superluminous Supernovae

Aysha Aamer[1,2], Matt Nicholl[1], Charlotte Angus[1], Shubham Srivastav[3], Jeff Cooke[4,5], Natasha Van Bemmel[4,5], Mark Suhr[4,5], Frédérick Poidevin[6,7], Stefan Geier[6,8], Joseph P. Anderson[9,10], Thomas de Boer[11], Kenneth C. Chambers[11], Ting-Wan Chen[12], Mariusz Gromadzki[13], Claudia P. Gutiérrez[14,15], Erkki Kankare[16], Réka Könyves-Tóth[17,18], Chien-Cheng Lin[11], Thomas B. Lowe[11], Eugene Magnier[11], Paolo Mazzali[19,20], Kyle Medler[11], Paloma Minguez[11], Tomás E. Müller-Bravo[21,22], and Ben Warwick[23]

[1] Astrophysics Research Centre, School of Mathematics and Physics, Queen's University Belfast, Belfast UK; aamer01@qub.ac.uk
[2] Department of Astronomy and Steward Observatory, University of Arizona, 933 North Cherry Avenue, Tucson, AZ 85721-0065, USA
[3] Astrophysics, Department of Physics, University of Oxford, Keble Road, Oxford OX1 3RH, UK
[4] Centre for Astrophysics and Supercomputing, Swinburne University of Technology, Hawthorn, VIC 3122, Australia
[5] ARC Centre of Excellence for Gravitational Wave Discovery (OzGrav), VIC 3122, Australia
[6] Instituto de Astrofísica de Canarias, Vía Láctea, 38205 La Laguna, Tenerife, Spain
[7] Universidad de La Laguna, Departamento de Astrofísica, 38206 La Laguna, Tenerife, Spain
[8] GRANTECAN, Cuesta de San José, s/n, 38712 Breña Baja, La Palma, Spain
[9] European Southern Observatory, Alonso de Córdova 3107, Casilla 19, Santiago, Chile
[10] Millennium Institute of Astrophysics MAS, Nuncio Monsenor Sotero Sanz 100, Office 104, Providencia, Santiago, Chile
[11] Institute for Astronomy, University of Hawaii, 2680 Woodlawn Drive, Honolulu, HI 96822, USA
[12] Graduate Institute of Astronomy, National Central University, 300 Jhongda Road, 32001 Jhongli, Taiwan
[13] Astronomical Observatory, University of Warsaw, Aleje Ujazdowskie 4, 00-478 Warszawa, Poland
[14] Institut d'Estudis Espacials de Catalunya (IEEC), Edifici RDIT, Campus UPC, 08860, Castelldefels, Barcelona, Spain
[15] Institute of Space Sciences (ICE), CSIC, Campus UAB, Carrer de Can Magrans, s/n, E-08193 Barcelona, Spain
[16] Department of Physics and Astronomy, University of Turku, 20014 Turku, Finland
[17] HUN-REN Research Centre for Astronomy and Earth Sciences, Konkoly Observatory, MTA Centre of Excellence, Konkoly Thege Miklós út 15-17, H-1121 Budapest, Hungary
[18] Department of Experimental Physics, Institute of Physics, University of Szeged, Dóm tér 9, Szeged 6720, Hungary
[19] Astrophysics Research Institute, Liverpool John Moores University, 146 Brownlow Hill, Liverpool L3 5RF, UK
[20] Max-Planck-Institut fur Astrophysik, Karl-Schwarzschild Straße 1, 85748 Garching, Germany
[21] School of Physics, Trinity College Dublin, The University of Dublin, Dublin 2, Ireland
[22] Instituto de Ciencias Exactas y Naturales (ICEN), Universidad Arturo Prat, Chile
[23] University of Warwick, Coventry CV4 7AL, UK
Received 2025 November 14; revised 2026 March 4; accepted 2026 March 9; published 2026 April 15

Abstract

Superluminous supernovae (SLSNe) are some of the brightest explosions in the Universe, representing the extremes of stellar deaths. At the upper end of their distribution is SN 2023taz, in a dwarf galaxy at $z = 0.407$. This is one of the most luminous SLSNe discovered to date with a peak absolute magnitude of $M_{g,\mathrm{peak}} = -22.75 \pm 0.03$ and a lower limit for energy radiated of $E = 2.9 \times 10^{51}$ erg. Magnetar model fits reveal individual parameter values typical of the SLSN population, but the combination of a low B-field and ejecta mass with a short spin period places SN 2023taz in a unusual region of parameter space, accounting for its extreme luminosity. The optical data around peak are consistent with a temperature of ∼17,000 K but SN 2023taz shows a surprising deficit in the UV compared to other events in this temperature range. We find no indication of dust extinction that could plausibly explain the UV deficit. The lower level of UV flux is reminiscent of the absorption seen in lower-luminosity events like SN 2017dwh, where Fe-group elements are responsible for the effect. However, in the case of SN 2023taz, there is no evidence for a larger amount of Fe-group elements which could contribute to line blanketing. Comparing to SLSNe with well-observed UV spectra, an underlying temperature of 8000–9000 K would match the UV spectral slope, but is not consistent with the optical color temperatures of these events. The most likely explanation is enhanced absorption by intermediate-mass elements, challenging previous findings that SLSNe exhibit similar UV absorption line equivalent widths. This highlights the need for expanded UV spectroscopic coverage of SLSNe, especially at early times, to build a framework for interpreting their diversity and to enable classification at higher redshifts where optical observations will exclusively probe rest-frame UV emission.

Unified Astronomy Thesaurus concepts: Core-collapse supernovae (304); Supernovae (1668); Massive stars (732)

Materials only available in the online version of record: data behind figure

1. Introduction

Superluminous supernovae (SLSNe) are a subset of extreme stellar explosions with luminosities that far exceed those of ordinary supernovae (SNe). The bolometric peaks for the most luminous of these explosions easily exceed 10^{44} erg s^{-1} (A. Gal-Yam et al. 2009; R. M. Quimby et al. 2011). This is up to 100 times greater than the peak reached by typical SNe.

These events cannot be explained by the radioactive decay of ^{56}Ni alone, which is the main power source invoked to explain other SNe. For SLSNe a ^{56}Ni-powered model would require Ni masses comparable to or greater than the total ejecta mass (e.g., C. Inserra et al. 2013). Instead the leading theories propose interaction with circumstellar material (CSM), or a magnetar central engine. Although the former is used to explain hydrogen-rich Type II SLSNe (N. Smith et al. 2007; A. J. Drake et al. 2010), both have been proposed for hydrogen-poor Type II SLSNe (hereafter just SLSNe) with the magnetar spin-down mechanism being widely adopted (e.g., C. Inserra et al. 2013; M. Nicholl et al. 2015; S. Gomez et al. 2024). Both mechanisms can reproduce the broad light curves, which require long diffusion timescales and therefore large ejecta masses, directly implicating massive progenitor stars. However, they imply very different progenitor systems and explosion physics. Disentangling these scenarios is critical for understanding SLSNe, probing the lives and deaths of the most massive stars, and the physical conditions of early star-forming environments.

The spectral energy distributions (SEDs) of SLSNe typically peak in the rest-frame u or near-UV bands, indicative of high temperatures (e.g., S. Gomez et al. 2024). However, in the UV, there are broad absorption lines from elements such as Mg, C, Si, and Fe, which dominate the spectra (L. Chomiuk et al. 2011; R. M. Quimby et al. 2011; D. A. Howell et al. 2013; P. M. Vreeswijk et al. 2014; L. Yan et al. 2018). These features are thought to be formed in the outer layers on the ejecta due to their high velocities (typically $>$10,000 km s^{-1}). Previous studies have shown that the UV spectra of SLSNe tend to exhibit similar equivalent widths (EWs) in their absorption lines, regardless of their luminosity (M. Nicholl et al. 2017b; L. Yan et al. 2017). Studies suggest that differing amounts of UV emission can generally be explained by varying power levels of a central energy source, rather than differences in absorbing column depths. This observation is consistent with a scenario where the continuum forms beneath the absorbing layer of fast-moving material, rather than in an external collision with CSM (M. Nicholl et al. 2017b).

At high redshifts ($z \gtrsim 1$), the rest-frame UV part of an SN spectrum is redshifted into the observer-frame optical. However, at these distances, the characteristic O II absorption features that are typically used to classify SLSNe are shifted to longer wavelengths where observations become increasingly challenging for ground-based telescopes (e.g., K. Barbary et al. 2009; J. Cooke et al. 2012; Y. C. Pan et al. 2017; M. Smith et al. 2018; C. Curtin et al. 2019). As a result, the detection and classification of SLSNe at high z must rely primarily on their rest-frame UV properties. Early discoveries revealed a surprisingly uniform class of SLSN spectra in the near-UV, particularly between 2000 and 3000 Å, suggesting that UV diagnostics could provide a reliable classification framework across a wide range of redshifts (M. Smith et al. 2018). With the advent of deeper, wide-field surveys, the number of SLSNe detected at high z is expected to increase dramatically (V. A. Villar et al. 2018). A few hundred SLSNe are now known, and spectroscopically confirmed from $z \sim 0.1$–2, with the majority at $z < 0.5$ (S. Gomez et al. 2024; A. Aamer et al. 2025). This growth is not solely due to the larger volumes being probed, but also because SLSNe may be more common in the early Universe, where the stellar mass distribution may be skewed toward more massive progenitors (J. Cooke et al. 2012). In addition, the binary fraction is thought to be higher at low metallicity (e.g., H. Sana et al. 2012). These binary interactions can significantly alter stellar evolution pathways through enhanced mass loss and changes in rotation rates, which may influence the formation rate of SLSNe (e.g., S. E. de Mink et al. 2013). This underpins the urgent need to build a detailed understanding of the connection between UV and optical properties of low-z SLSNe, as this will be essential for interpreting the large samples of high-z SLSNe expected from upcoming surveys.

In this paper we present SN 2023taz, one of the brightest SLSNe to date at optical wavelengths, but with a deficit in the near-UV compared to other SLSNe with similar color temperatures in the optical. This challenges our current understanding of UV diversity in SLSNe and raises important questions about the central engine model, as well as our ability to identify SLSNe at high redshifts. The paper is structured as follows. Section 2 presents the data collected for this object. The host galaxy for this event is analyzed in Section 3. Section 4 discusses the analysis of the light curves, and Section 5 looks at the modeling of the light curves and the inferred parameters of the system. Section 6 discusses the analysis of the spectra. We discuss the possible scenarios for this object in Section 7. Lastly we present our conclusions in Section 8.

All magnitudes reported in this paper are given in the AB system. A flat ΛCDM cosmology is also assumed throughout with $H_0 = 70\,\mathrm{km\,s^{-1}\,Mpc^{-1}}$ and $\Omega_\Lambda = 0.7$.

2. Observations

2.1. Discovery and Classification

SN 2023taz was first detected by the Panoramic Survey Telescope and Rapid Response System (Pan-STARRS; K. C. Chambers et al. 2016) on 2023 September 12 under the internal name PS23ila at a magnitude $m_w = 20.36$ mag. This followed a deep upper limit 3 days prior at $m_w \gtrsim 21.8$ mag. It was later reported by the Asteroid Terrestrial-impact Last Alert System (ATLAS) project (J. L. Tonry et al. 2018) on 2023 October 6 under the name ATLAS23tqv with a magnitude of $m_c = 19.14$ mag, and by the Zwicky Transient Facility (ZTF; E. C. Bellm et al. 2019) on 2023 December 6 under the name ZTF23abgzmfs with a magnitude of $m_g = 20.03$ mag. The event has an R.A. and decl. (J2000) of $19^{\mathrm{h}}28^{\mathrm{m}}23\overset{\mathrm{s}}{.}01$ and $-04°54'43\overset{''}{.}86$, respectively.

The object was chosen for classification by the Advanced Public ESO Spectroscopic Survey of Transient Objects (ePESSTO+; S. J. Smartt et al. 2015) based on the lack of a visible host and a long light-curve rise. A spectrum obtained with the ESO New Technology Telescope (NTT) on 2023 November 4 was consistent with a young SLSN (A. Aamer et al. 2023). A redshift of $z = 0.42$ was determined using the SUPERNOVA IDENTIFICATION code (S. Blondin & J. L. Tonry 2007). This is a spectral cross-correlation tool used to classify SNe by comparing observed spectra against a library of template spectra across various types and phases. Reexamination of the spectrum shows narrow [O III] λλ4959, 5007 and Hβ host galaxy lines at a redshift $z = 0.407 \pm 0.005$. We therefore adopt this latter value for the analysis in this paper. This gives a luminosity distance of $D_L = 2239$ Mpc. The corresponding absolute magnitude at the time of discovery is

Table 1
Photometric Filters Used within This Paper and Their Effective Central Wavelength

Filter	Central Wavelength (Å)	Telescope
z	8670	LCOGT
i	7503, 7471, 7946.21	Pan-STARRS, LCOGT, NTT
o	6630	ATLAS
r	6150, 6656.65	LCOGT, NTT
w	5981	Pan-STARRS
c	5182	ATLAS
g	4648, 5105	LCOGT, NTT
u	3543	LCOGT
W1	2716	Swift
M2	2247	Swift
W2	2076	Swift

Note. The filter profiles have been obtained from the Spanish Virtual Observatory Filter Profile Service (C. Rodrigo et al. 2012, 2024; C. Rodrigo & E. Solano 2020).

therefore $M_w = -21.4$ mag, firmly placing SN 2023taz in the regime of SLSNe.

2.2. Photometry

Photometry for SN 2023taz was obtained from a number of telescopes. The filters used and their effective central wavelengths are provided in Table 1.

Data in *c* and *o* bands were collected from the ATLAS forced photometry server (J. L. Tonry et al. 2018; K. W. Smith et al. 2020; L. Shingles et al. 2021), and in *g* and *r* bands from the Lasair ZTF forced photometry server (F. J. Masci et al. 2019), both of which are performed on difference images. For the ATLAS data, observations were binned to a daily cadence. Pan-STARRS photometry in *w* and *i* bands was derived using the Pan-STARRS Image Processing Pipeline (E. A. Magnier et al. 2020).

Follow-up observations were also coordinated in *ugriz* with the Las Cumbres Observatory (LCOGT). Within their network, several 1 m telescopes were used across multiple observatories. These images were reduced using the BANZAI pipeline (C. McCully et al. 2018). Late-time photometry was obtained using the ESO NTT in *gri* with the ESO Faint Object Spectrograph and Camera (EFOSC2). This was done through the ePESSTO+ collaboration.

All photometry on raw frames for the LCOGT and NTT data was carried out using the PHOTOMETRY-SANS-FRUSTRATION Python package, which performs point-spread function (PSF) photometry using Astropy and Photutils (M. Nicholl et al. 2023). The frames are calibrated using the Pan-STARRS catalog (H. A. Flewelling et al. 2020) in order to obtain zero-points. For the *u*-band images, zero-points were calculated using the SkyMapper catalog (C. A. Onken et al. 2024), with aperture photometry performed on reference stars within a cone of 10′ from the target. Although the late-time NTT observations resulted in 3σ detections, the measured magnitudes are mainly consistent with marginal detections of (or upper limits on) the host galaxy in preexplosion Pan-STARRS imaging (see Section 3).

The Neil Gehrels Swift Observatory (Swift; N. Gehrels et al. 2004) was also triggered to observe SN 2023taz beginning on 2023 November 10 using the UV Optical Telescope (UVOT; P. W. A. Roming et al. 2005), in the UV filters. However the SN was only detected in one epoch, in one filter, with the rest providing upper limits. The individual frames in each filter were coadded using `uvotimsum` within the HEASOFT package. Photometry was performed on the final frames using the `uvotsource` task with a 5″ aperture, following the procedure outlined in T. S. Poole et al. (2008) and P. J. Brown et al. (2009). The measured count rates were converted to AB magnitudes using the UVOT photometric zero-points (T. S. Poole et al. 2008; A. A. Breeveld et al. 2011).

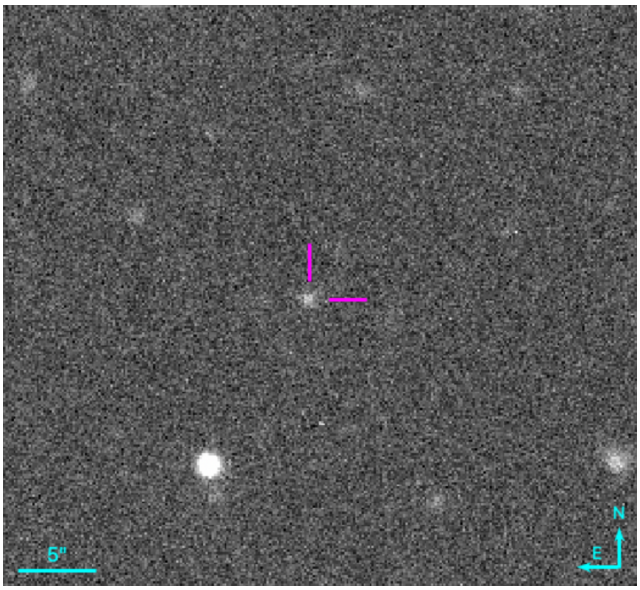

Figure 1. Host galaxy of SN 2023taz, as detected in LRIS *g*-band imaging at a phase of +481 days.

Late-time imaging of the putative host galaxy was obtained using the Low Resolution Imaging Spectrometer (LRIS; J. B. Oke et al. 1995; C. C. Steidel et al. 2004) on 2025 August 31 at a phase of +481 days postpeak. The host was clearly detected in both filters (see Section 3). Figure 1 shows the *g*-band imaging of the host. LRIS is a two-arm instrument and the field was imaged with 3×60 s integrations (180 s total exposure time per filter) in the *g* band using the blue arm and the *i* band using the red arm simultaneously by employing the D560 dichroic. Twilight sky images were taken for flat-fielding. However, "supersky" flat-field images for both filters were preferred and created by median-combining dithered images from two different fields using *g*– and *i*-band filters separately. The images were aligned, stacked, and processed using conventional IRAF routines. Photometry was performed using Source Extractor (E. Bertin & S. Arnouts 1996), and the zero-points corrected by crossmatching nearby stars to measured values in the DECam Local Volume Exploration Survey (A. Drlica-Wagner et al. 2021) catalog.

2.3. Spectroscopy

Spectra for SN 2023taz were obtained through ePESSTO+ using the NTT/EFOSC2 spectrograph. Spectra were taken using the Gr#13 grism, which observes between 3685–9315 Å. However, the data from 2023 November 6 were taken using both the Gr#11 and the Gr#16 grisms, which range from 3380–7520 Å and 6015–10320 Å, respectively. The spectra were first reduced using the PESSTO

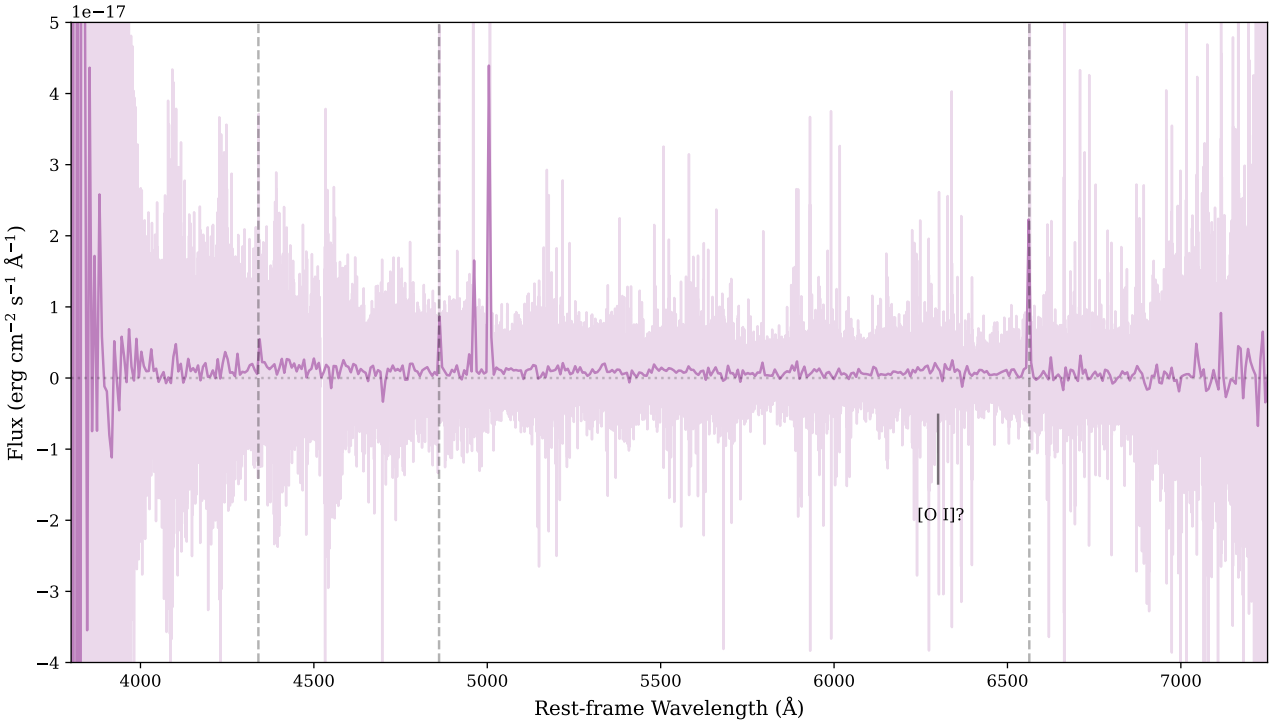

Figure 2. Spectrum of SN 2023taz obtained with X-shooter in the visible arm at a phase of +310.6 days postpeak. The spectrum has also been smoothed using a Savitzky–Golay filter, as shown in dark purple. Host galaxy emission lines from the Balmer series are highlighted with gray dashed lines. A possible line identification for [O I] λλ6300, 6364 is highlighted. A dotted horizontal line is plotted at zero flux.

pipeline (S. J. Smartt et al. 2015), which applies debiasing, flat-field correction, trace extraction, wavelength calibration, and flux calibration using standard stars observed with identical setups. A spectrum was also obtained on the Nordic Optical Telescope (NOT) on 2024 December 11 with the Alhambra Faint Object Spectrograph and Camera (ALFOSC). The observation consisted of three integrations of 1000 s using the Grism#4 and a slit aperture of 1.″3. A standard reduction and calibration of the spectrum was conducted using `Pypeit` (J. Prochaska et al. 2020).

All spectra were then processed to remove tellurics using the Python package TELLURICS-BEGONE[24] (E. J. Ridley et al. 2024). They were then corrected for foreground extinction using the ASTROPY (Astropy Collaboration et al. 2018) implementation of the K. D. Gordon et al. (2023) extinction law. This law combines previous extinction relations (K. D. Gordon et al. 2009, 2021; E. L. Fitzpatrick et al. 2019; M. Decleir et al. 2022) to provide a single relationship across 912 Å–32 μm. The value of reddening used was $E(B-V) = 0.0152$ (E. F. Schlafly & D. P. Finkbeiner 2011). The spectra were also flux corrected by scaling linearly to the closest photometry in the g, r, and i bands. Lastly, the spectra were redshift corrected. For visual clarity, the [O III] λλ4959, 5007 host emission lines were removed by fitting a Gaussian centered on each wavelength within a 20 Å range, and subtracting them off. Spectra taken on the same night have been coadded, and all spectroscopic observations are listed in Table 2. The full spectral sequence and corresponding analysis are presented in Section 6.

A late-time spectrum was obtained on 2025 January 2 using X-shooter on the VLT (see Figure 2). The UV, visible, and IR arms had total exposure times of 2440 s, 2560 s, and 2600 s, respectively. The data were then processed using the `soxspipe` package (D. R. Young & M. Landoni 2023), and corrected for Milky Way (MW) extinction. We recover a continuum at signal-to-noise ratio (SNR) < 1 between 5000 and 6000 Å, and cannot detect any clear transient features within the spectrum.

Extinction from the host galaxy was assumed to be negligible and has not been corrected for. This is based on the observed Balmer decrement (see Section 3), as well as the observed colors and systematic studies of SLSN host galaxies, which show negligible or no host extinction (e.g., D. A. Perley et al. 2016; S. Schulze et al. 2018).

3. Host Galaxy

A faint galaxy designated Pan-STARRS1 Object J030.8220-23.6798 is reported in the Pan-STARRS1 (PS1) stacked object catalog in all of the g, r, i, z, and y bands, with a mean offset of 0.″54 from the position of SN 2023taz. We assume that this is the host galaxy. However the detection is only significant at the 3σ level in r band, with a PSF magnitude of $m_{r,\mathrm{host}} = 22.90 \pm 0.19$ mag and a Kron magnitude of $m_{r,\mathrm{host}} = 22.99 \pm 0.26$ mag. The measurement in g is just below the threshold with a PSF magnitude of $m_{g,\mathrm{host}} = 23.99 \pm 0.32$ mag, and no corresponding Kron magnitude. The measured magnitudes in i and z are less certain, with visual inspection of the images using the PS1 image cutout server showing no clear source at the position of the transient in these filters. This places limits of $m_{i,\mathrm{host}} > 23.1$ mag and $m_{z,\mathrm{host}} > 22.3$ mag. Instead the LRIS images obtained at a phase of +481 days postpeak were used to measure the host galaxy magnitude at $m_{i,\mathrm{host}} = 23.20 \pm 0.08$ mag and $m_{g,\mathrm{host}} = 23.97 \pm 0.09$ mag in the i and g bands, respectively. The r-band photometry of SN 2023taz has been host subtracted using the Pan-STARRS flux measurement, and

[24] https://github.com/EJRidley/tellurics-begone

the g and i bands have been host subtracted using the LRIS flux measurements. For the early phases of the light curves (before $\sim$100 days), we also apply host subtraction in the z band. As the host detection is marginal, it does not make a significant difference to the light curves, as the SN flux dominates at these phases.

A galaxy K-correction calculator was used to calculate the absolute magnitudes of the host (I. V. Chilingarian et al. 2010; I. V. Chilingarian & I. Y. Zolotukhin 2012). Using this we estimate absolute magnitudes of $M_{g,\mathrm{host}} = -18.40 \pm 0.32$ mag and $M_{r,\mathrm{host}} = -18.92 \pm 0.19$ mag. We can compare these to a sample of 27 SLSN host galaxies from S. Schulze et al. (2018) for hosts with $z \lesssim 0.5$. They show a mean value of $M_B = -17.10 \pm 0.30$ mag for hosts with a mean redshift of $z = 0.24$. The g-band host magnitude of SN 2023taz is therefore at the brighter end of SLSN hosts in this redshift range. However, S. Schulze et al. (2018) also find that the host galaxies tend to be brighter at higher redshifts, so this difference may simply reflect the fact that SN 2023taz lies at a higher redshift than the mean of the sample. The host galaxy color $g - r \approx 0.5$ is consistent with other SLSN hosts at a similar redshift (R. Lunnan et al. 2014), suggesting it is a star-forming galaxy consistent with typical SLSN hosts.

A late-time spectrum was obtained at a phase of +310.6 days using X-shooter. The results from the visible arm are shown in Figure 2 and clearly show the narrow host galaxy emission lines. This spectrum shows very little SN signal except potentially a small bump $\sim$6300 Å, which corresponds to the well-observed nebular emission line of [O I] $\lambda\lambda$6300, 6364. However, the signal is too weak for a definitive identification. The flux from the Balmer emission lines was measured by integrating over the emission profile. The continuum was determined by randomly sampling 100 points in the regions on either side of the line to obtain a median value for the continuum and its associated uncertainty. From this we find values of $\mathrm{H}\alpha = (1.78 \pm 0.11) \times 10^{-16}$ erg s^{-1} cm^{-2}, $\mathrm{H}\beta = (5.88 \pm 0.45) \times 10^{-17}$ erg s^{-1} cm^{-2}, and $\mathrm{H}\gamma = (2.42 \pm 0.34) \times 10^{-17}$ erg s^{-1} cm^{-2}. These yield Balmer decrements of $\mathrm{H}\alpha/\mathrm{H}\beta = 3.03 \pm 0.29$, and $\mathrm{H}\gamma/\mathrm{H}\beta = 0.41 \pm 0.07$. As the spectrum was corrected for MW extinction, any residual extinction present would be from the host and local environment of the SN. These values are consistent with the expected ratios for in a scenario with no extinction (D. E. Osterbrock & G. J. Ferland 2006).

The Hα emission line can also be used as a diagnostic for the star formation rate (SFR) within a galaxy, assuming a Salpeter initial mass function (R. C. Kennicutt 1998). This yields a value of $\mathrm{SFR} = 0.85 \pm 0.05\, M_\odot\, \mathrm{yr}^{-1}$. This SFR is consistent with the sample of hosts from G. Leloudas et al. (2015) where a range of 0.01–6.04 $M_\odot$ yr^{-1} was found.

4. Light Curves

The light curves for SN 2023taz spanning over 200 days are presented in Figure 3. The rise and peak of the light curves are detected at high SNR in the w-band data from Pan-STARRS. This is a broadband filter covering g, r, and i with an effective wavelength close to that of r (or to rest-frame g band at the redshift of SN 2023taz). To find the time of maximum light, we fit a second-degree polynomial and found a time of peak of MJD 60241 at an apparent magnitude $w_{\mathrm{peak}} = 19.07$ mag. Using the first spectrum obtained on MJD 60252.3, we perform a K-correction and find an absolute magnitude of $M_{g,\mathrm{peak}} = -22.75 \pm 0.03$ mag (also corrected for foreground extinction of $A_V = 0.039$ mag; E. F. Schlafly & D. P. Finkbeiner 2011). This is at the upper extreme of SLSN luminosities. Z. H. Chen et al. (2023) find a median peak luminosity of $M_{g,\mathrm{med}} = -21.48^{+1.13}_{-0.61}$ mag from their sample of 78 SLSNe from ZTF, making this event more than 2σ brighter than the average ZTF SLSN. More recently S. Gomez et al. (2024) analyzed a sample of 262 SLSNe, from which the median peak rest-frame g-band absolute magnitude is measured to be $M_{g,\mathrm{med}} = -21.5^{+1.0}_{-0.6}$ mag, consistent with the ZTF sample. SN 2023taz is once again outside of the 2σ range and is in fact brighter in the g band than all events within both samples.

Figure 3 shows the bluer bands fading much faster than the redder bands after peak, as the SN cools. This can be quantified by the time taken for the SN to fade by a factor of e from peak in each band (τ_e). This e-folding decline time is $\tau_{e,g} = 44$ days and $\tau_{e,o} = 82$ days in the g and o bands, respectively. This is comparable to the average decline time found in S. Gomez et al. (2024) of $\tau_{e,r} = 44^{+38}_{-18}$ days. This measurement also assumes that the first g-band point in the light curve is close to or at peak. The rapid cooling of SN 2023taz also resulted in mostly UV nondetections.

4.1. Colors

The color evolution of SN 2023taz is shown in Figure 4. This is compared to the model light curves of a subset of events from S. Gomez et al. (2024) with observations in each respective band. Within the sample, there are 44, 43, and 42 events with photometry in W1, M2, and W2, respectively. The photometry for SN 2023taz was first K-corrected using the SLSNE Python package (S. Gomez et al. 2024) to ensure consistent color comparisons between objects. The colors in the g and UVOT bands with respect to r band were then determined by subtracting the closest r-band magnitude. In all cases, the phase differences were less than 1.5 days. The $g - r$ color starts off similar to the population average with $g - r \sim -0.3$ mag at peak. It then evolves smoothly to redder colors before settling at $g - r \sim 0.8$ mag. This late-time optical color is somewhat redder than typical SLSNe. However, the UV–optical colors are the reddest in the population especially at early times. The triangles in the UV bands represent lower limits for the color in each subplot. We can see this event is redder than average across the entire time span where UV photometry was obtained. It is especially apparent between 0 and 20 days where the lower limits are constraining. The single W1 detection places tight constraints on the color $\mathrm{W1} - r = 1.83 \pm 0.23$ mag at 12 days postpeak. At 12 days postpeak, the median and 1σ spread for the modeled events are $W1 - r = -0.73^{+0.39}_{-0.26}$ mag for the subset of events with W1 photometry. This means the detection at that phase is more than 5σ away from the median, pushing it to extremes of the population. Therefore, SN 2023taz stands alone among the current sample as a highly luminous SLSN, with a very red UV–optical color.

In comparison Gaia16apd, an SLSN with a comparable peak bolometric luminosity and optical light-curve timescale, displays a much bluer color than SN 2023taz (T. Kangas et al. 2017; M. Nicholl et al. 2017b; L. Yan et al. 2017). Its $g - r$ color is initially comparable, but its UV colors are bluer by $\sim$4 mag. This is not simply a consequence of Gaia16apd having a higher temperature. As shown in Figure 5, we find similar best-fitting blackbodies for the optical photometry of

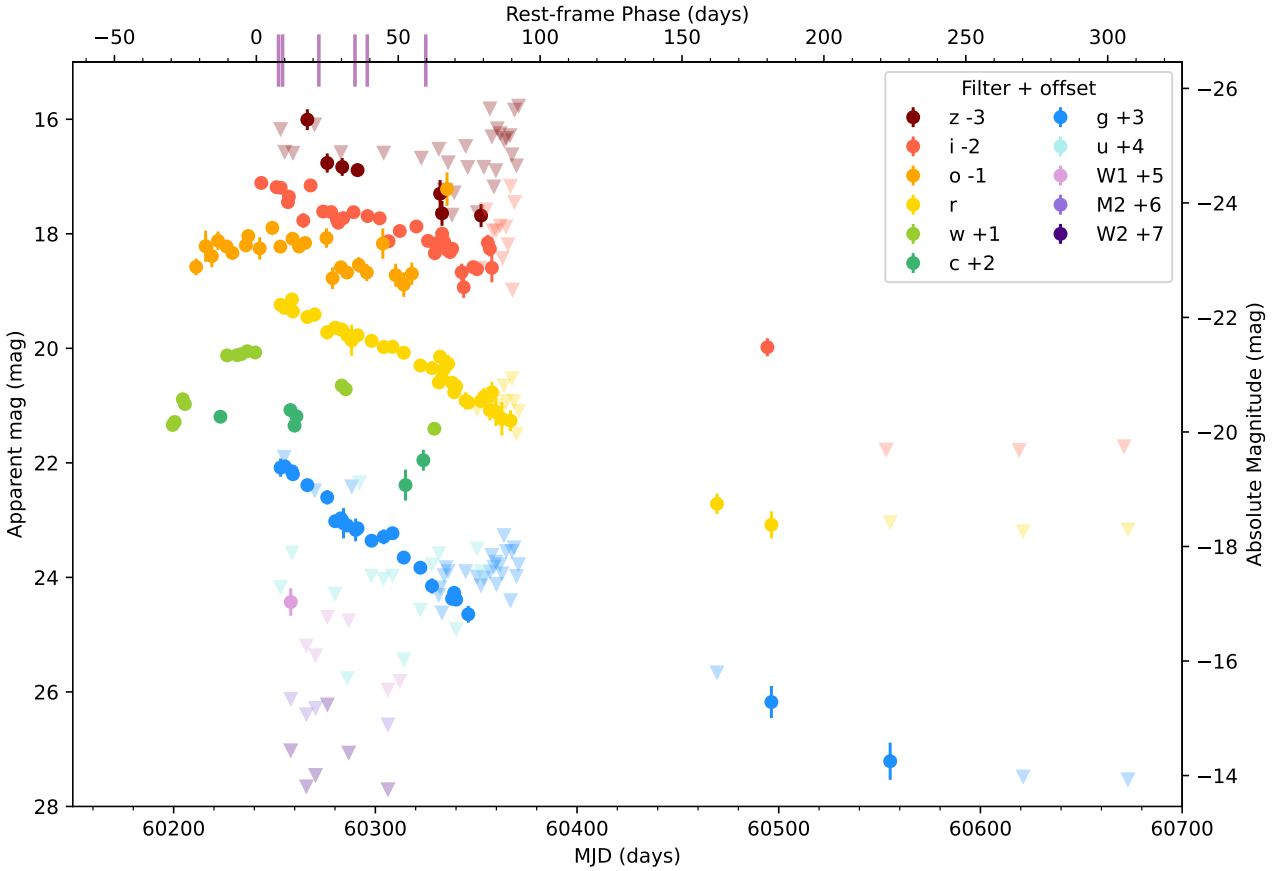

Figure 3. The light curves of SN 2023taz, with all magnitudes in the AB system and corrected for MW extinction. Phases are given in rest-frame days relative to the *w*-band maximum. The figure compiles photometric data from ATLAS, Pan-STARRS, ZTF, Swift, LCOGT, and NTT. MJD is in the observer frame, with 3σ upper limits marked as inverted triangles. For clarity, ATLAS *c*- and *o*-band points are shown without upper limits and have been binned to a daily cadence. Vertical tick marks on the top axis indicate the epochs of the spectra displayed in Figure 10. The compilation of detected light-curve data is available as the data behind the figure. (The data used to create this figure are available in the online article.)

Gaia16apd and SN 2023taz. Therefore, the difference in $UV - r$ colors of several magnitudes between these events seems to indicate a difference in their UV properties. The reddest SLSN from the S. Gomez et al. (2024) sample in $g - r$ at late times is SN 2017dwh (P. K. Blanchard et al. 2019). This event is similar to the general population at early times around peak, before diverging quickly and becoming much redder with a color $g - r = 1$ mag by 30 days postpeak. There are no UV observations of this event, and therefore a comparison cannot be made for the UV colors. However, its spectrum shows evidence for strong Fe-group absorption in the near-UV (P. K. Blanchard et al. 2019); see Section 6.

4.2. Blackbody Parameters

The blackbody parameters for this analysis were calculated using the SUPERBOL Python package (M. Nicholl 2018). This is a tool designed to derive bolometric light curves and fit blackbody models to the observed photometry. It works by constructing the SED at each epoch, integrating this to determine the optical luminosity, and fitting a blackbody curve to estimate the temperature, radius, and unobserved UV–near-IR luminosity of the emitting source. In this case, a modified blackbody (based on M. Nicholl et al. 2017c and L. Yan et al. 2018) was fit to the photometry. This suppresses the SED below a given wavelength following the form

$$f_\lambda(T, R) = \begin{cases} \left(\dfrac{\lambda}{\lambda_0}\right)^{\alpha} f_{\lambda,\mathrm{BB}}(T, R) & \text{for } \lambda < \lambda_0, \\ f_{\lambda,\mathrm{BB}}(T, R) & \text{for } \lambda > \lambda_0. \end{cases} \quad (1)$$

Here f_λ is the flux at a given wavelength λ, α is the suppression index, λ_0 is a cutoff wavelength for the suppression, and $f_{\lambda,\mathrm{BB}}$ is the normal blackbody spectrum without any modifications applied. We use values of $\alpha = 1.56$ and $\lambda_0 = 3072$ Å based on our light-curve modeling (Section 5). The SEDs were also shifted into the rest frame. We used the *w* and *r* bands as reference points to anchor the color evolution, allowing SUPERBOL to infer the colors of the other bands either by assuming a constant color evolution, or by interpolating unevenly sampled photometry using a polynomial.

Integrating under the SED at each epoch also gives the bolometric luminosity at each point in time. By integrating this luminosity across the entire observed span of the SN, we estimate the total radiated energy is $E > 2.9 \times 10^{51}$ erg. This value represents a lower limit, as it does not account for incomplete temporal and wavelength coverage, nor any emission occurring outside the span of our photometric observations. This energy is consistent with the typical

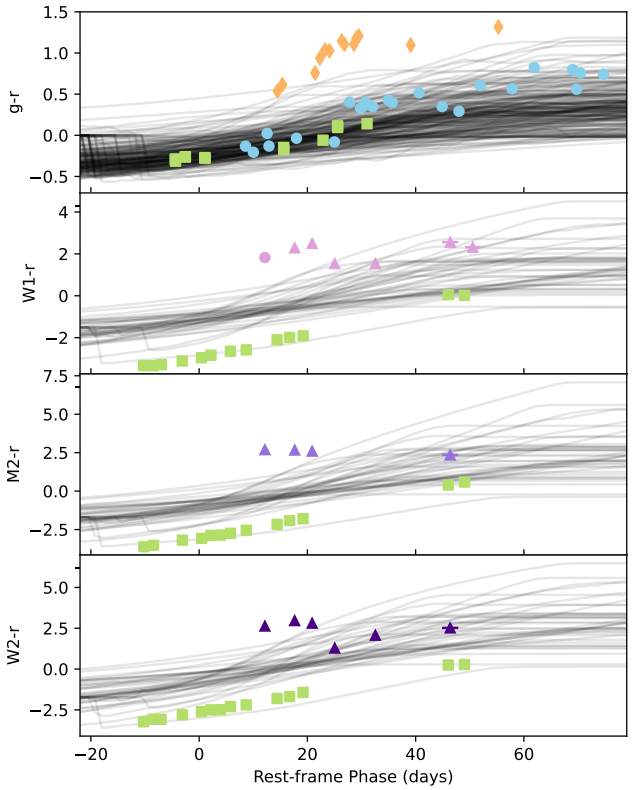

Figure 4. Photometric colors for SN 2023taz in blue, pink, purple, and indigo compared to the colors from the sample of model fits to SLSNe photometry in S. Gomez et al. (2024) shown in black. Measurements are given in AB mag with lower limits denoted by triangles. Photometric colors for Gaia16apd (T. Kangas et al. 2017; M. Nicholl et al. 2017b; L. Yan et al. 2017) and SN 2017dwh (P. K. Blanchard et al. 2019) are also plotted in green squares and orange diamonds, respectively. Phases are given relative to peak.

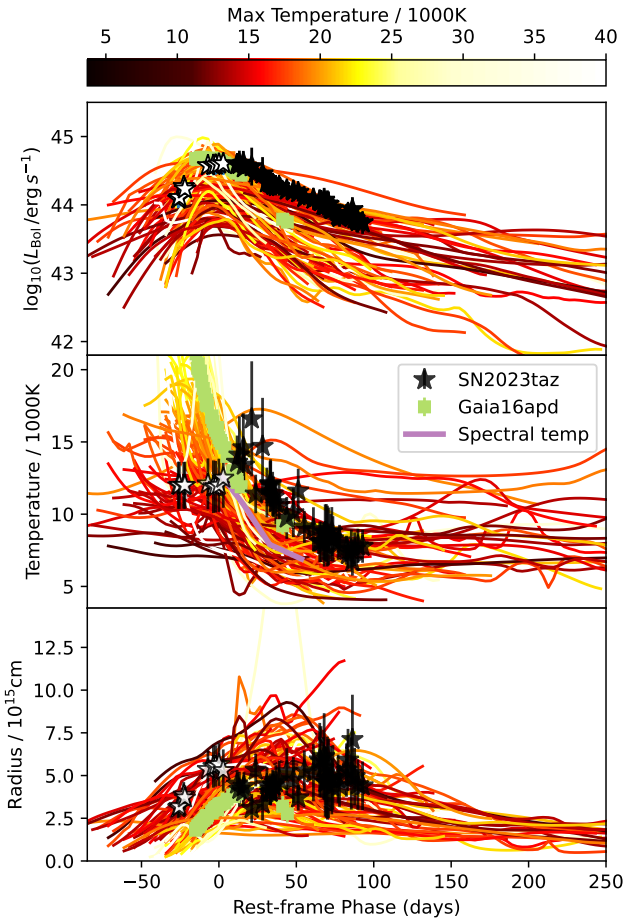

Figure 5. Parameters derived from SED fits of the light curves. Unfilled stars indicate where fewer than three bands were available for the fit. The colors of each line correspond to the peak blackbody temperature calculated for each event from the sample in S. Gomez et al. (2024), and shown in the color bar at the top. The parameters for Gaia16apd are plotted in green squares. Top: bolometric luminosity. Middle: blackbody temperature. The temperature from blackbody fits to the spectra are also plotted in purple. Bottom: blackbody radius.

energies radiated by SLSNe ranging between $\sim 5 \times 10^{49}$ and 5×10^{51} erg (S. Gomez et al. 2024).

Figure 5 shows the blackbody parameters in comparison to the full sample of events from S. Gomez et al. (2024). We also highlight Gaia16apd on this plot. The unfilled stars represent the early light curve of SN 2023taz, where there is only coverage in the w, c, and o bands. Since w is effectively $c + o$, this means there is only a small part of the SED covered and therefore the blackbody fits are not reliable.

In the top panel of Figure 5, we can see that the bolometric luminosity for this event is at the upper extreme of the population. At peak it has a bolometric luminosity of $L_{\rm bol} = (4.1 \pm 1.7) \times 10^{44}\,{\rm erg\,s^{-1}}$. At late times SN 2023taz remains within the 1σ range of the sample. It is also interesting to note that the brighter events tend to be the hottest, as evidenced by the color scaling on the figure.

The middle panel of Figure 5 shows the temperature evolution of the sample of events as estimated from these SED fits. SN 2023taz reaches a peak temperature of $16{,}600 \pm 4000$ K, at 10 days after the bolometric peak. However hotter events at peak also cool quicker. This corresponds to the rapid spectral change between the "hot" photospheric phase and the "cool" photospheric phase as outlined in R. M. Quimby et al. (2018) and A. Aamer et al. (2025). Plotted on the same subfigure in purple is the temperature derived from fitting a blackbody curve to the spectra of SN 2023taz (see Section 6). In comparison, Gaia16apd starts off at a much hotter temperature of $\sim$22,000 K with a much more rapid decline to $\sim$15,000 K at peak. At this point the temperatures are comparable and shows that the UV–optical color differences seen after peak in Section 4.1 are not driven by different temperatures. The temperatures of both events are at the higher end but well within the 1σ range of the population.

From the blackbody fits to the SED we can also calculate the size of the photospheric radius with time. SN 2023taz has a slow rise to peak radius, reaching a maximum radius of $R = (6.1 \pm 2.5) \times 10^{15}$ cm around 60 days postpeak. In comparison, Gaia16apd has a much smaller maximum radius, which peaks soon after maximum light. However, at the peak of the light curve, both events have similar-sized radii. As the temperature evolution of both events postpeak is similar, this larger radius explains why the light curve of SN 2023taz is much longer lived.

5. Magnetar Parameters

SLSNe show a wide range of luminosities and timescales. This requires a mechanism that decouples the magnitude of the heating source from its duration, and is largely independent of the ejecta properties. The simplest model that achieves this is

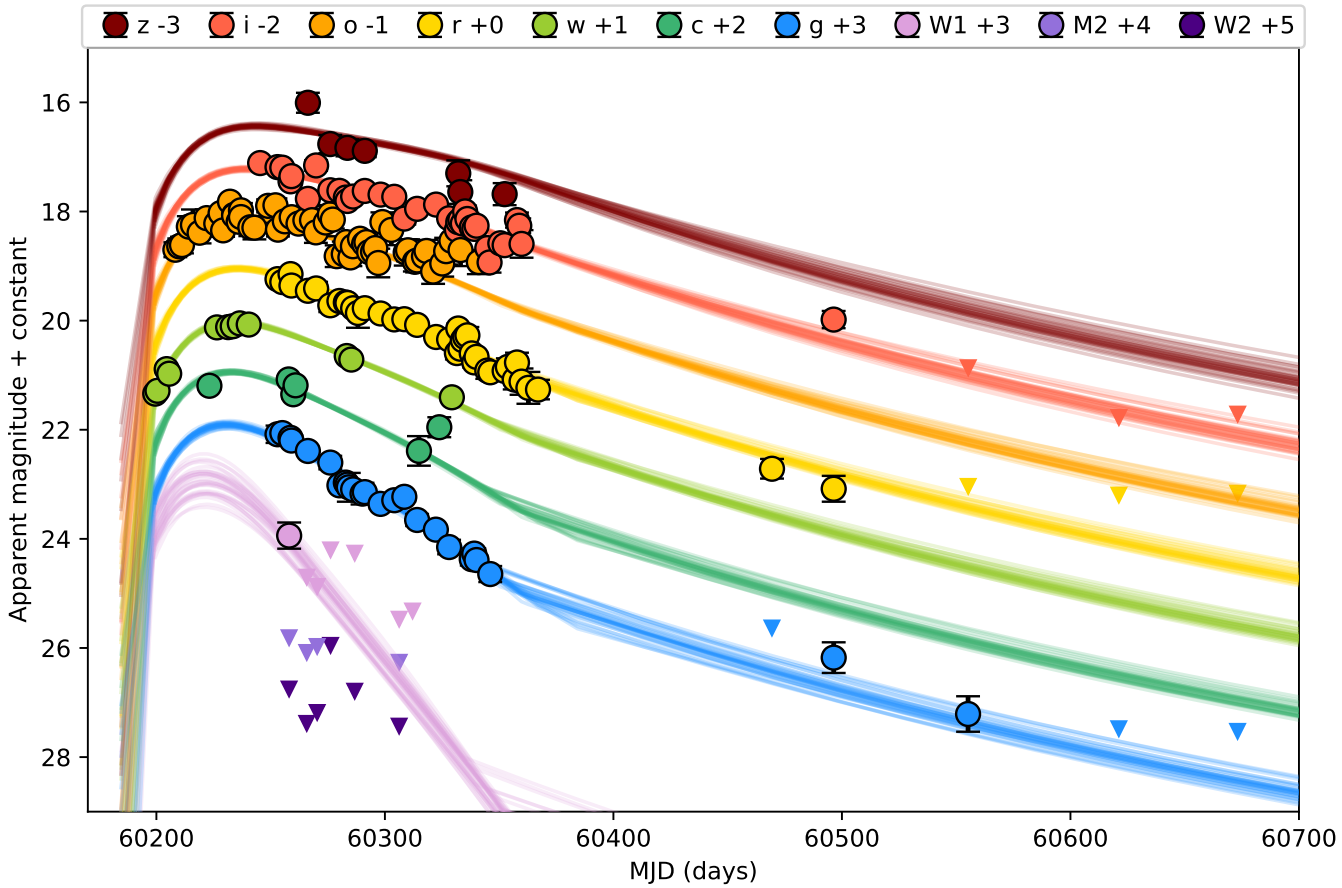

Figure 6. MOSFIT fits to the light curves of SN 2023taz using the `slsnni` model. This model combines a magnetar engine with a flexible level of contribution from the radioactive decay of ^{56}Ni. Upper limits are indicated via inverted triangles.

the magnetar central engine model, which reproduces the bulk features of large SLSN samples (D. Kasen & L. Bildsten 2010; P. A. Mazzali et al. 2016; M. Nicholl et al. 2017c; S. Gomez et al. 2024) mainly through variations in spin period (heating rate), magnetic field (heating duration), and ejecta mass (diffusion timescale). As SN 2023taz stands out as one of the brightest SLSNe to date, it is interesting to determine which features of the model would lead to such a bright (and relatively long-lived) event. While other power sources may be applicable to SLSNe, fitting SN 2023taz within the same framework as other events enables more general insights, and fitting the multicolor photometry allows us to test whether it is subject to anomalous extinction compared to other events.

To explore the central engine properties, we modeled the multicolor light curves using the Modular Open Source Fitter for Transients (MOSFIT; J. Guillochon et al. 2018). Specifically we used the `slsnni` model, which models a magnetar internal engine following M. Nicholl et al. (2017c), while allowing a contribution from the radioactive decay of ^{56}Ni as a free parameter. The model assumes a modified blackbody in the form of Equation (1), with λ_0 and α set as free parameters. This model has been widely applied to SLSNe (S. Gomez et al. 2024) and shown to reproduce their overall light-curve properties. For this work, we adopt the default set of priors, following the approach of S. Gomez et al. (2024).

The best-fit MOSFIT model light curves are shown in Figure 6. The rise and peak in the o and w bands are well captured, as well as the decline in all bands. The exception to this is the z band, where the model consistently overpredicts the luminosity, even at early times. This discrepancy may arise from an unconstrained host contribution that was not subtracted (see Section 3). Although it was assumed that the host flux would be negligible compared to the SN at these early phases, this may have nevertheless affected the model fits. Although we show UVOT upper limits in the plot, we only include the single epoch with a detection in UVW1 in our fit, as the model struggles to fit the optical light curves and the deep UV limits simultaneously. The inability for the model to fit the data could indicate that the simple suppressed blackbody SED model does not fully account for strong line absorption in the UVOT UVM2 and UVW2 bands.

The best-fit parameters for the `slsnni` model are shown in Figure 7. These parameters are mostly within the 1σ range of the population sample from S. Gomez et al. (2024), including the spin period at $P_{\rm spin} = 2.25^{+0.33}_{-0.36}$ ms just below the sample mean at $P_{\rm spin,mean} = 2.4^{+3.0}_{-1.2}$ ms. A lower value of $P_{\rm spin}$ results in a more luminous event. The value for the perpendicular component of the magnetic field to the spin axis, $\log(B_\perp/{\rm G}) = 13.73^{+0.13}_{-0.14}$, is also just within the median and 1σ range of values in S. Gomez et al. (2024) of $\log(B_{\perp,{\rm mean}}/{\rm G}) = 14.2 \pm 0.4$. The effect of a lower value for $B_\perp$ is a longer magnetar spin-down timescale.

In our host galaxy and photospheric temperature analyses we assumed negligible extinction from the host galaxy. This is supported by the Balmer decrement in the host galaxy spectrum. It is also supported by the posterior of our light-curve model fit, which independently fits the host extinction through the parameter for column density in the host ($n_{\rm H,host}$).

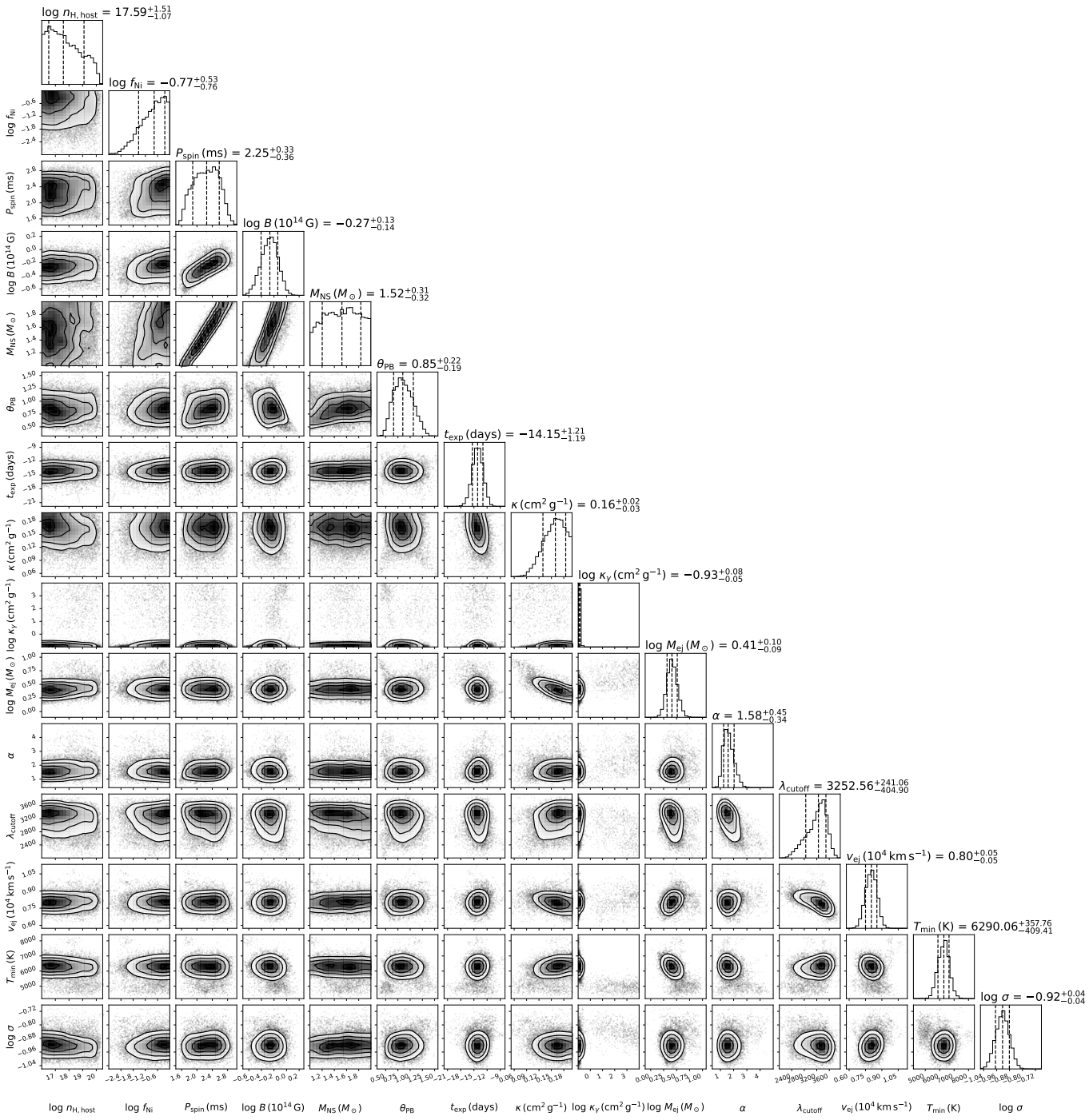

Figure 7. Corner plot of the posteriors for the `slsnni` model fit to the light curves of SN 2023taz. Median and 1σ ranges are labeled.

The fits favored $n_{\rm H,host} \leqslant 18\,{\rm cm}^{-2}$, which corresponds to an extinction $A_V < 10^{-3}$ mag (T. Güver & F. Özel 2009).

The model also estimates the fraction of ^{56}Ni ($f_{\rm Ni}$) in the ejecta required in addition to the contribution from the magnetar. This resulted in a value of $f_{\rm Ni} = 17.0\%^{+40.5\%}_{-14.0\%}$. We can combine this with the mass ejected parameter ($M_{\rm ej} = 2.57^{+0.66}_{-0.48}\,M_\odot$) to find that the mass of ^{56}Ni ejected is $M_{\rm Ni} \sim 0.4\,M_\odot$ and could be as high as $M_{\rm Ni} \sim 1\,M_\odot$ based on the upper end of the uncertainty range. The fraction (and hence the mass) is not well constrained because the model prefers the magnetar as the primary heating source, and a ^{56}Ni mass up to $\sim$0.4 $M_\odot$ has little effect on the magnetar-powered light curve. To confirm this, we ran another fit with a fixed $f_{\rm Ni} = 0\%$, which resulted in very similar fits and posteriors. This is consistent with the findings in S. Gomez et al. (2024) where most SLSNe do not require a significant contribution from radioactive decay to power them.

Figure 8 shows the evolution of the heating rate, using the best-fit spin period ($P_{\rm spin} = 2.25$ ms), magnetic field ($B_\perp = 5.37 \times 10^{13}$ G) and neutron star mass ($M_{\rm NS} = 1.52\,M_\odot$) from MOSFIT. The heating rate follows an initial plateau lasting $\sim$1.5 days, followed by a steep decay with a power-law index of 2. The energy input is very similar whether or not a contribution from ^{56}Ni is included, demonstrating that

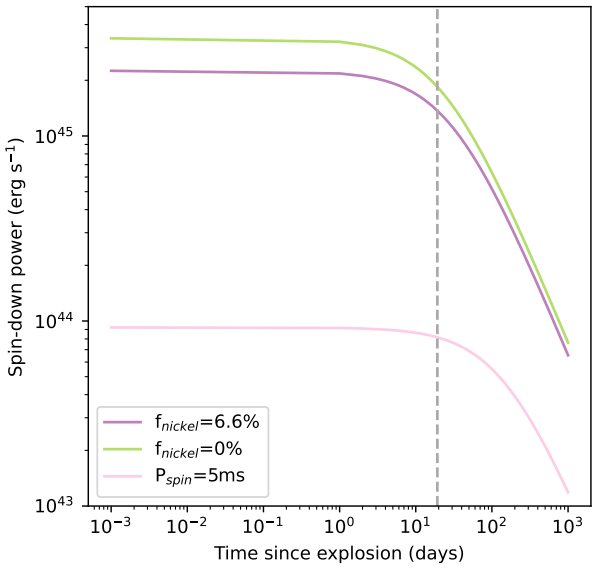

Figure 8. Magnetar spin-down energy based on the best-fitting parameters when allowing the nickel fraction to vary in the models, as well as when the nickel fraction is fixed to 0%. In pink is the spin-down energy using the same parameters as the flexible nickel model but setting the spin period to a larger value of 5 ms.

SN 2023taz can easily be powered without a substantial contribution from radioactive decay.

Still in Figure 8, we mark the time of bolometric peak with a vertical dashed line. The time of peak here is measured by averaging the bolometric light curves produced by 100 walkers from the MOSFIT output. The rise time measured for this event is $t_{\rm rise} = 26$ days, close to the median value found by S. Gomez et al. (2024) of $t_{\rm rise,all} = 27^{+25}_{-13}$ days. At peak luminosity, the observed radiated luminosity is comparable to the rate of energy input from the central engine (W. D. Arnett 1982). Figure 8 demonstrates that at the time of peak in SN 2023taz, the energy injection of the magnetar remains high, and the spin-down power has not yet transitioned to the steep decline of the power-law tail. This is a consequence of the low $B_\perp$ value discussed earlier, which extends the spin-down timescale. The sustained energy injection up to the time of peak is what drives SN 2023taz to be a very luminous SLSN (M. Nicholl et al. 2017c).

Figure 9 shows the distribution of $B_\perp$ and $M_{\rm ej}$ values from S. Gomez et al. (2024), with points colored by their $P_{\rm spin}$ values. We can see that SN 2023taz falls below the bulk of the population both in terms of ejecta mass, and B-field, lying on the edge of the joint distribution. The effect of a low $M_{\rm ej}$ is to reduce the rise time, and in this case matching it to the spin-down timescale. However, other SLSNe occupy a similar region in $M_{\rm ej}$–$B_\perp$ space, and are generally less luminous than SN 2023taz. The reason is that most of these events have longer spin periods $\gtrsim$4 ms, as shown by the color scale. SN 2023taz stands out by having a shorter spin period than most other objects in a similar region of the parameter space. This has a dramatic effect, as the magnetar peak spin-down rate scales as $P_{\rm spin}^{-4}$. We demonstrate the effect of spin period in Figure 8 by plotting the spin-down energy for a hypothetical event with the same $B_\perp$ as SN 2023taz, but a longer spin period of $P_{\rm spin} = 5$ ms. This results in a slightly longer spin-down time, but with a much lower level of energy throughout, resulting in a less luminous peak.

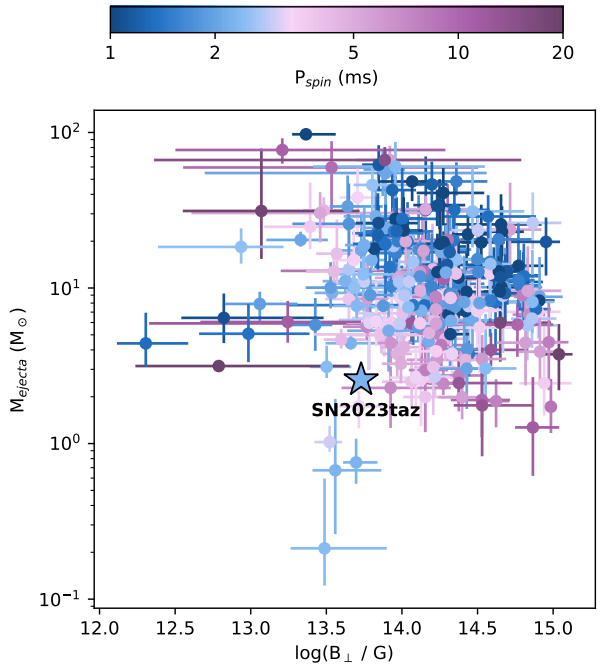

Figure 9. The perpendicular component of the magnetic field ($B_\perp$ against the ejecta mass ($M_{\rm ej}$) for the sample of SLSNe from S. Gomez et al. (2024). The points are also colored by their spin period ($P_{\rm spin}$). The values derived for SN 2023taz are plotted with a star shape.

Table 2
Spectroscopic Observations of SN 2023taz

Date	MJD	Phase (days)	Grism	Exposure Time (s)	Telescope
04-11-2023	60252.3	8.0	Gr#13	900	NTT
06-11-2023	60254.0	9.3	Gr#16	2700	NTT
06-11-2023	60254.1	9.3	Gr#11	2700	NTT
24-11-2023	60272.1	22.1	Gr#13	2700	NTT
09-12-2023	60287.1	32.8	Gr#13	2700	NTT
11-12-2023	60289.9	34.8	#4	3 × 1000	NOT
18-12-2023	60296.1	39.2	Gr#13	2700	NTT
18-12-2023	60296.2	39.2	Gr#13	2700	NTT
16-01-2024	60325.1	59.7	Gr#13	2700	NTT
16-01-2024	60325.1	59.8	Gr#13	2700	NTT
30-06-2024	60491.4	177.9	Gr#13	2700	NTT
30-06-2024	60491.4	178.0	Gr#13	2700	NTT
30-06-2024	60491.4	178.0	Gr#13	2700	NTT
06-07-2024	60497.3	182.2	Gr#16	2700	NTT
06-07-2024	60497.4	182.2	Gr#16	2700	NTT
02-01-2025	60678.1	310.6	⋯	2600	VLT

Note. Phase is given in rest-frame days with respect to the time of maximum light in the o band. Observations are obtained either on the NTT telescope using the EFOSC2 instrument, on the NOT with the ALFOSC instrument, or using X-shooter on the Very Large Telescope (VLT).

6. Spectral Evolution

Figure 10 presents the postmaximum spectroscopic evolution of SN 2023taz. The spectra at early times are dominated by a hot, blue continuum, with relatively weak absorption features from O II superimposed. The spectral coverage extends to 53 days postpeak, by which point the SN has transitioned from the hot photospheric phase to the cooler photospheric stage. The spectra still exhibit underlying

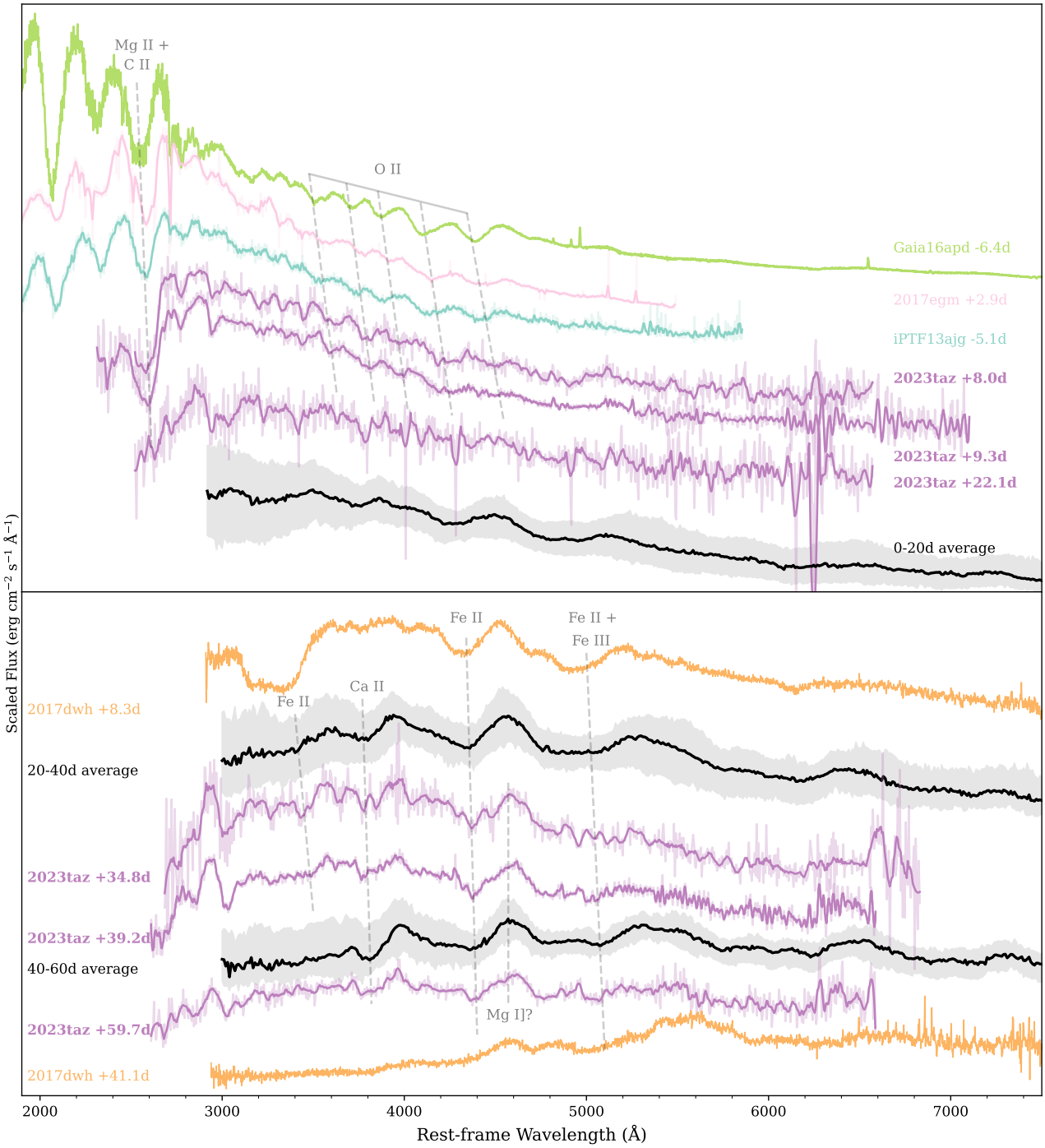

Figure 10. The spectral evolution of SN 2023taz is shown in purple. The spectra have also been smoothed using a Savitzky–Golay filter, as shown in dark purple. Comparison spectra of Gaia16apd, SN 2017egm, iPTF13ajg, and SN 2017dwh are also plotted. Average spectra from a sample of 234 events are plotted in black (A. Aamer et al. 2025). Line identifications are highlighted with gray dashed lines.

continuum emission, but with O II replaced by O I, Mg I, Fe II, and Ca II. These two distinct phases are split into the top and bottom panel of Figure 10, respectively. Unfortunately, the coverage does not extend to the nebular phase of this object.

Blackbody models were also fit to these spectra, and included in Figure 5. For the two spectra just after peak, the fits were trimmed to only include wavelengths above 2800 Å. This was done due to the deep UV absorption line just below this cutoff, which interfered with the fits and forced a lower temperature fit that did not capture the shape in the optical. Applying a modified blackbody fit did not alter the temperatures significantly, with a largest deviation of ∼700 K. These temperatures are slightly lower than those from the broadband SED fitting, but this may be due to the spectra not extending as far blue and therefore not capturing the peak of the SED well. This means we are only fitting to the Rayleigh–Jeans tail in these spectra, making the temperature much harder to constrain.

Examining the early spectra at 8–22 days after peak, in the optical we can see the O II absorption lines blueshifted with a velocity of 6000 km s^{-1}. This is lower than typical line velocities measured for other SLSNe, typically around

10,000–15,000 km s^{-1} (e.g., R. M. Quimby et al. 2018; A. Gal-Yam 2019). The lines are also quite weak compared to the continuum. The formation of the O II lines was found to be temperature dependent, with the classic "W" shape appearing for temperatures in the range 14,000–16,000 K (R. Könyves-Tóth 2022; R. Könyves-Tóth & B. Seli 2023; S. Saito et al. 2024). From SED fitting in Section 4.2 we can see that the temperatures at the phases of these spectra are below this threshold, explaining the weaker O II lines.

We show line identifications in Figure 10 extending into the near-UV. Here, we can see a broad absorption line with a minimum at 2672 Å. This line has been attributed to Mg II $\lambda\lambda$2798, 2803 (L. Chomiuk et al. 2011; R. M. Quimby et al. 2011) with a possible contribution from C II (D. A. Howell et al. 2013; P. M. Vreeswijk et al. 2014; P. A. Mazzali et al. 2016).

Figure 10 also shows average SLSN spectra in different time bins, constructed by A. Aamer et al. (2025) based on a sample of 234 SLSNe. Comparisons have been plotted with phases corresponding to the phases of SN 2023taz. We can see that during the hot photospheric phase, the spectra show a optical continuum shape that is similar to the average SLSN, though the lines in SN 2023taz appear much narrower. This is partially due to artificial line broadening in the average spectrum from averaging many events with different velocities. Comparisons to individual objects such as iPTF13ajg (P. M. Vreeswijk et al. 2014), SN 2017egm (S. Dong et al. 2017; M. Nicholl et al. 2017a; D. Xiang et al. 2017; S. Bose et al. 2018; W. Lin et al. 2023; J. Zhu et al. 2023), and Gaia16apd (T. Kangas et al. 2017; M. Nicholl et al. 2017b; L. Yan et al. 2017) also show that this event looks overall similar to a typical SLSN but confirm the lower velocities. These comparison spectra were selected because their optical continua have similar temperatures and slopes to SN 2023taz.

By 30 days postpeak, SN 2023taz has transitioned to the cooler photospheric stage with more prominent emission lines and P Cygni profiles, as shown in the lower panel of Figure 10. At these latter phases we can make a more direct comparison to the average spectra from A. Aamer et al. (2025). We see many similarities in both the overall shape of the underlying continuum and in the specific lines. There are visible P Cygni profiles from a blend of Fe II around ∼3600 Å, Ca II $\lambda\lambda$3934, 3968, and a weak feature at ∼6300 Å possibly due to [O I] λ6355. The feature around 4500 Å is likely due to a blend of Fe II with possible contributions from Mg I] λ4571. However, we note there are weaker Fe features around 5500 Å compared to the population average.

7. Investigation of the UV Deficit

We have established SN 2023taz to be an SLSN that is very luminous but otherwise quite typical in the optical. Its most surprising feature is the very red UV–optical color. We now discuss possible physical origins.

Figure 4 indicated a UV flux deficit at early times, using the UV–optical colors. We confirm this in the top panel of Figure 11 using the early spectra of SN 2023taz and comparison events with UV data from Figure 10. Although SN 2023taz, Gaia16apd, SN 2017egm, and iPTF13ajg all show quite similar optical spectra, the fluxes diverge in the UV.

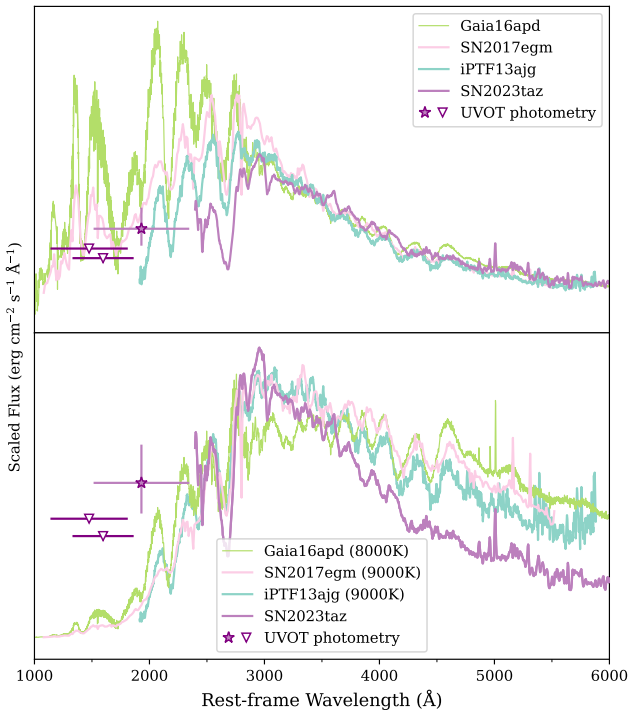

Figure 11. UV spectral comparisons for SN 2023taz, Gaia16apd, SN 2017egm, and iPTF13ajg. The UVOT photometry for SN 2023taz are the measurements taken closest to peak. Photometric upper limits are indicated by inverted triangles. Top: observed optical and UV spectra around maximum light. The optical sections of the spectra are comparable between the three events, but they diverge in the UV, particularly in the depth of the Mg II $\lambda\lambda$2798, 2803 feature. Bottom: the spectra for Gaia16apd, SN 2017egm, and iPTF13ajg have been warped to blackbody temperatures of 8000 K, 9000 K, and 9000 K, respectively. These temperatures were chosen to match the continuum shape around the Mg II UV absorption line to that observed in SN 2023taz. However, after this warping to match the near-UV, neither the optical continuum shapes nor the far-UV fluxes are consistent with SN 2023taz, showing that temperature differences alone cannot explain the differences in the near-UV colors. Moreover, after matching the UV continuum levels it is apparent that the EW of the Mg II absorption line is significantly greater in SN 2023taz.

7.1. Extinction

One possible cause of a redder UV–optical SED is extinction. Extinction curves of the MW include a prominent bump thought to be due to the presence of graphite or polycyclic aromatic hydrocarbons (B. T. Draine 2003). This broad feature spans over 1000 Å centered at 2175 Å and therefore would effect the observed flux in a wavelength range corresponding roughly to the UVOT UVM2 filter. However, at $z = 0.407$, an observer-frame wavelength of 2175 Å corresponds to only ∼1500 Å in the SN rest frame, so it cannot explain the suppression we see at longer rest-frame wavelengths of ∼2000–3000 Å (Figure 11).

Although the data have been corrected for foreground extinction, host galaxy extinction was neglected in our SED analysis in Section 4. Analysis of the host galaxy spectrum (Section 3) suggested that this was negligible, but to further confirm this we also check for Na I D absorption lines within the spectrum, which are often used a tracer for line-of-sight dust extinction (D. Poznanski et al. 2012). We find no evidence for Na I absorption within the series of spectra. The lack of absorption places limits on the extinction to <0.1 mag based on the relation from D. Poznanski et al. (2012). The high temperatures needed to match the optical-only color

temperature for SN 2023taz also indicate that extinction is unlikely to be the mechanism for the UV suppression, as this would work to redden the whole spectrum.

Taken together, the lack of Na I absorption, the faint host, the MOSFIT modeling, the color temperature evolution, and the Balmer decrements all lead to the same conclusion: extinction from the host galaxy or local environment is negligible, and dust extinction cannot be the primary cause of the UV suppression in SN 2023taz.

7.2. Temperature

One explanation for the lower UV flux levels could be due to a lower temperature (though as discussed in Section 4.2 the temperature measured from the optical data appears fairly typical). To investigate this in more detail, we scaled the spectra of Gaia16apd, SN 2017egm, and iPTF13ajg to match the UV continuum shape on either side of the Mg II line in SN 2023taz. This is done by dividing the spectra by the best-fit blackbody temperature ($\sim$17,000 K, $\sim$14,000 K, and $\sim$15,000 K, respectively), and multiplying by a new blackbody with a lower temperature following the methodology in M. Nicholl et al. (2017b). We show the results of these transformations in the bottom panel of Figure 11. This allows us to test how much cooler these SLSNe would need to be in order to reproduce the near-UV colors of SN 2023taz. Achieving a match to the UV spectrum between 2500 and 3000 Å in SN 2023taz required scaling Gaia16apd to a temperature of 8000 K, and SN 2017egm and iPTF13ajg both to a temperature of 9000 K. Although the continuum shape can be reproduced by the lower temperature, the depth of the Mg II line is difficult to reproduce. The warped spectra also have a much lower flux at $\sim$2000 Å than SN 2023taz. Most importantly, scaling to a cooler continuum also vastly alters the optical SEDs, which no longer resemble SN 2023taz. The spectra are also no longer physically self-consistent, as the dominant O II lines would not form at these lower temperatures. From this we can conclude that the colors of SN 2023taz cannot be self-consistently reproduced by simply warping a typical SLSN spectrum to a cooler temperature.

7.3. Absorption

Having ruled out extinction or a cooler photosphere as the cause of the unusually red colors of SN 2023taz, we are left to consider enhanced UV line absorption as an explanation for the observed UV deficit.

Another object that showed a flux deficit in the UV compared to most SLSNe is SN 2017dwh. However, as shown in Figure 4, this event also had a much redder $g - r$ color than SN 2023taz. The spectra in Figure 10 show that the reason for this is enhanced absorption from Fe-group elements, which can be seen with the broad absorption trough from Co II at $\sim$3200 Å in the spectrum at +8.31 days (P. K. Blanchard et al. 2019). This transitions to more of an overall line blanketing in the spectrum at +41.05 days, which can be seen by the extremely red spectral shape. However, in the case of SN 2023taz we do not see evidence for a large amount of Fe-group elements both from the lack of Fe II emission $\sim$5500 Å, but also the lack of absorption seen from this Co II line. Instead another explanation is needed to explain this level of UV absorption.

The warping in Figure 11 indicated that enhanced absorption by intermediate-mass elements such as Mg could account for some of the UV deficit. To quantify the strength of the UV line absorption, we measured the pseudo-EW =of the broad absorption feature centered around 2670 Å, attributed primarily to Mg II with possible contributions from C II. We estimated the continuum as a straight line between the blue and red peaks of the feature and integrated the fractional depth. We find EW(Mg II) $\approx$ 75 Å for SN 2023taz, compared to 47 Å, 51 Å, and 44 Å for Gaia16apd, SN 2017egm, and iPTF13ajg, respectively in the rest frame. In SN 2023taz, this absorption feature is significantly stronger, appearing $\sim$50% more pronounced.

Assuming the line is not saturated, the EW scales with the column density of the absorbing element. The implication is that SN 2023taz has a larger quantity of intermediate-mass elements, particularly Mg, above the photosphere at this epoch. This could be the result of several factors. In typical SLSN models, Mg is produced in the ashes of explosive carbon burning. If the progenitor was highly stripped, with most of the He and some of the C layers removed, this could allow Mg-rich layers to be visible closer to the surface. However, the deficit appearing at shorter UV wavelengths (around 2400 Å), where strong carbon lines are expected (P. M. Vreeswijk et al. 2014; L. Yan et al. 2017), makes this scenario less likely, as it would require both more Mg and C.

Alternatively, the UV suppression could reflect enhanced mixing of Mg into the outer ejecta. One possible way to increase mixing is a powerful central engine that drives fluid instabilities (K.-J. Chen et al. 2016, 2020; A. Suzuki et al. 2021). This would be consistent with the high luminosity of SN 2023taz, though it raises the question of why a similar effect is not seen in Gaia16apd, a similarly luminous (if shorter-lived) event.

A third possibility is that the photosphere in SN 2023taz has receded further by peak light, into a deeper Mg-rich zone. This is consistent with the low expansion velocities measured from the O II lines, but perhaps in tension with the high luminosity, which would typically sustain a more extended photosphere.

We cannot distinguish definitively between these scenarios, but all suggest that the red UV–optical color in SN 2023taz is best explained by unusually strong UV line blanketing rather than differences in temperature or extinction. Obtaining spectroscopy of future SLSNe further into the UV will help to illuminate the reason.

8. Conclusions

The analysis in this paper focused on the SLSN SN 2023taz, presenting optical and UV photometry and spectra obtained across a period of over 300 days. This event is one of the brightest SLSNe to date with an absolute magnitude of $M_{g,\mathrm{peak}} = -22.75 \pm 0.03$ mag, and an estimated energy radiated of $E = 2.9 \times 10^{51}$ erg. Light-curve modeling indicates that the parameters required in the central engine theory are not individually atypical, but when combined place SN 2023taz in a unusual region of parameter space with $P_{\mathrm{spin}} = 2.25^{+0.33}_{-0.36}$ ms, $\log(B_{\perp}/\mathrm{G}) = 13.73^{+0.13}_{-0.14}$, and $M_{\mathrm{ej}} = 2.57^{+0.66}_{-0.48}\,M_{\odot}$. In the magnetar framework, SLSNe achieve high luminosities when the spin-down timescale of the central engine and the photon diffusion timescale of the ejecta are well matched, or when the magnetar is born spinning near its maximal rotation rate. In the

case of SN 2023taz, both of these conditions are met, placing it near the upper end of the SLSN luminosity distribution.

SED fits to the multicolor light curves indicate high temperatures reaching a peak of 16,600 ± 4000 K just after peak. Despite this high peak temperature, the UV color of this event is the reddest observed for an SLSNe with a color UVW1 − $r = 1.83 \pm 0.23$ compared to the population average at this phase of $UVW1 - r = -0.73^{+0.39}_{-0.26}$. This is despite a relatively normal $g - r$ color evolution compared to the population.

Taking SLSNe with well-observed UV spectra and warping these to match the UV spectral shape of SN 2023taz require temperatures of ∼8000–9000 K, inconsistent with the shapes of their optical SEDs. This shows that a lower temperature than other SLSNe cannot explain the UV deficit. Moreover, there is no evidence for significant extinction in SN 2023taz, and comparison to SN 2017dwh showed that iron line blanketing does not produce the observed spectral shape. The EW of the Mg II absorption feature around 2800 Å in SN 2023taz is measured to be 75 Å, significantly larger than in Gaia16apd, SN 2017egm, and iPTF13ajg, which have EWs of $\lesssim$50 Å, suggesting that the UV deficit is most likely due to a higher column density of Mg and potentially other intermediate-mass elements.

Future surveys like LSST will find large numbers of SLSNe, but the increase in detection rate comes from the ability of deeper surveys to detect more distant events. LSST will detect ∼10,000 SLSNe per year out to $z \sim 3$ (V. A. Villar et al. 2018). However, beyond $z \gtrsim 1$, optical observations will probe only rest-frame UV emission, and beyond $z \gtrsim 4$ near-IR observations will probe the rest-frame UV. Thus photometric identification and spectroscopic classification will be required based on rest-frame UV (K. Barbary et al. 2009; J. Cooke et al. 2012; Y. C. Pan et al. 2017; M. Smith et al. 2018; C. Curtin et al. 2019). The case of SN 2023taz highlights that SLSNe may exhibit greater diversity in their UV properties than previously appreciated, even when appearing typical in the optical. This underlines the critical need for joint UV–optical observations of low-redshift SLSNe. Understanding how UV diversity correlates with optical features will be essential to reliably identify and characterize these events as we move into an era of high-redshift transient surveys.

Acknowledgments

A.A., M.N., and C.A. are supported by the European Research Council (ERC) under the European Union's Horizon 2020 research and innovation program (grant agreement No. 948381) and by UKSA/STFC grant No. ST/Y000692/1.

J.C. and N.V.B. acknowledge funding from the Australian Research Council Discovery Project DP200102102 and the Australian Research Council Centre of Excellence for Gravitational Wave Discovery (OzGrav), CE170100004 and CE230100016.

F.P. acknowledges support from the Spanish Ministerio de Ciencia, Innovación y Universidades (MICINN) under grant No. PID2022-141915NB-C21.

T.-W.C. acknowledges the financial support from the Yushan Fellow Program by the Ministry of Education, Taiwan (MOE-111-YSFMS-0008-001-P1) and the National Science and Technology Council, Taiwan (NSTC grant 114-2112-M-008-021-MY3).

C.P.G. acknowledges financial support from the Secretary of Universities and Research (Government of Catalonia) and by the Horizon 2020 Research and Innovation Programme of the European Union under the Marie Skłodowska-Curie and the Beatriu de Pinós 2021 BP 00168 program, from the Spanish Ministerio de Ciencia e Innovación (MCIN), the Agencia Estatal de Investigación (AEI) 10.13039/501100011033 under the PID2023-151307NB-I00 SNNEXT project, from Centro Superior de Investigaciones Científicas (CSIC) under the PIE project 20215AT016, the program Unidad de Excelencia María de Maeztu CEX2020-001058-M, and from the Departament de Recerca i Universitats de la Generalitat de Catalunya through the 2021-SGR-01270 grant.

R.K.T. acknowledges support by the NKFIH/OTKA FK-134432 grant of the National Research, Development and Innovation (NRDI) Office of Hungary.

T.E.M.B. is funded by Horizon Europe ERC grant No. 101125877.

B.W. is supported by UKRI's STFC studentship grant funding, project reference ST/X508871/1.

Based on observations collected at the European Organisation for Astronomical Research in the Southern Hemisphere, Chile, under ESO program 114.27AG.001, and as part of ePESSTO+ (the advanced Public ESO Spectroscopic Survey for Transient Objects Survey—PI: Inserra), under ESO program IDs 112.25JQ.

This work has made use of data from the Asteroid Terrestrial-impact Last Alert System (ATLAS) project. ATLAS is primarily funded to search for near earth asteroids through NASA grants NN12AR55G, 80NSSC18K0284, and 80NSSC18K1575; by-products of the NEO search include images and catalogs from the survey area. The ATLAS science products have been made possible through the contributions of the University of Hawaii Institute for Astronomy, the Queen's University Belfast, the Space Telescope Science Institute, and the South African Astronomical Observatory.

The Pan-STARRS1 Surveys (PS1) have been made possible through contributions of the Institute for Astronomy, the University of Hawaii, the Pan-STARRS Project Office, the Max-Planck Society and its participating institutes, the Max Planck Institute for Astronomy, Heidelberg and the Max Planck Institute for Extraterrestrial Physics, Garching, The Johns Hopkins University, Durham University, the University of Edinburgh, Queen's University Belfast, the Harvard-Smithsonian Center for Astrophysics, the Las Cumbres Observatory Global Telescope Network Incorporated, the National Central University of Taiwan, the Space Telescope Science Institute, the National Aeronautics and Space Administration under grant No. NNX08AR22G issued through the Planetary Science Division of the NASA Science Mission Directorate, the National Science Foundation under grant No. AST-1238877, the University of Maryland, and Eotvos Lorand University (ELTE).

Based on observations made with the Nordic Optical Telescope (NOT), owned in collaboration by the University of Turku and Aarhus University, and operated jointly by Aarhus University, the University of Turku and the University of Oslo, representing Denmark, Finland and Norway, the University of Iceland, and Stockholm University at the Observatorio del Roque de los Muchachos, La Palma, Spain, of the Instituto de Astrofisica de Canarias. The data presented here were obtained with ALFOSC, which is provided by the

Instituto de Astrofisica de Andalucia (IAA) under a joint agreement with the University of Copenhagen and NOT.

This research made use of the "K-corrections calculator" service available at http://kcor.sai.msu.ru/.

This research has made use of the SVO Filter Profile Service "Carlos Rodrigo," funded by MCIN/AEI/10.13039/501100011033/ through grant PID2023-146210NB-I00.

ORCID iDs

Aysha Aamer https://orcid.org/0000-0002-9085-8187
Matt Nicholl https://orcid.org/0000-0002-2555-3192
Shubham Srivastav https://orcid.org/0000-0003-4524-6883
Frédérick Poidevin https://orcid.org/0000-0002-5391-5568
Stefan Geier https://orcid.org/0000-0003-3154-2120
Joseph P. Anderson https://orcid.org/0000-0003-0227-3451
Kenneth C. Chambers https://orcid.org/0000-0001-6965-7789
Ting-Wan Chen https://orcid.org/0000-0002-1066-6098
Mariusz Gromadzki https://orcid.org/0000-0002-1650-1518
Claudia P. Gutiérrez https://orcid.org/0000-0003-2375-2064
Erkki Kankare https://orcid.org/0000-0001-8257-3512
Réka Könyves-Tóth https://orcid.org/0000-0002-8770-6764
Chien-Cheng Lin https://orcid.org/0000-0002-7272-5129
Thomas B. Lowe https://orcid.org/0000-0002-9438-3617
Eugene Magnier https://orcid.org/0000-0002-7965-2815
Paolo Mazzali https://orcid.org/0000-0001-6876-8284
Kyle Medler https://orcid.org/0000-0001-7186-105X
Paloma Minguez https://orcid.org/0009-0003-8803-8643
Ben Warwick https://orcid.org/0009-0005-8379-3871

References

Aamer, A., Moore, T., Ramsden, P., et al. 2023, TNSAN, 289, 1
Aamer, A., Nicholl, M., Gomez, S., et al. 2025, MNRAS, 541, 2674
Arnett, W. D. 1982, ApJ, 253, 785
Astropy Collaboration, Price-Whelan, A. M., Sipőcz, B. M., et al. 2018, AJ, 156, 123
Barbary, K., Dawson, K. S., Tokita, K., et al. 2009, ApJ, 690, 1358
Bellm, E. C., Kulkarni, S. R., Graham, M. J., et al. 2019, PASP, 131, 018002
Bertin, E., & Arnouts, S. 1996, A&AS, 117, 393
Blanchard, P. K., Nicholl, M., Berger, E., et al. 2019, ApJ, 872, 90
Blondin, S., & Tonry, J. L. 2007, ApJ, 666, 1024
Bose, S., Dong, S., Pastorello, A., et al. 2018, ApJ, 853, 57
Breeveld, A. A., Landsman, W., Holland, S. T., et al. 2011, AIPC, 1358, 373
Brown, P. J., Holland, S. T., Immler, S., et al. 2009, AJ, 137, 4517
Chambers, K. C., Magnier, E. A., Metcalfe, N., et al. 2016, arXiv, arXiv:1612.05560
Chen, K.-J., Woosley, S. E., & Sukhbold, T. 2016, ApJ, 832, 73
Chen, K.-J., Woosley, S. E., & Whalen, D. J. 2020, ApJ, 893, 99
Chen, Z. H., Yan, L., Kangas, T., et al. 2023, ApJ, 943, 41
Chilingarian, I. V., Melchior, A.-L., & Zolotukhin, I. Y. 2010, MNRAS, 405, 1409
Chilingarian, I. V., & Zolotukhin, I. Y. 2012, MNRAS, 419, 1727
Chomiuk, L., Chornock, R., Soderberg, A. M., et al. 2011, ApJ, 743, 114
Cooke, J., Sullivan, M., Gal-Yam, A., et al. 2012, Natur, 491, 228
Curtin, C., Cooke, J., Moriya, T. J., et al. 2019, ApJS, 241, 17
Decleir, M., Gordon, K. D., Andrews, J. E., et al. 2022, ApJ, 930, 15
de Mink, S. E., Langer, N., Izzard, R. G., Sana, H., & de Koter, A. 2013, ApJ, 764, 166
Dong, S., Bose, S., Chen, P., et al. 2017, ATel, 10498, 1
Draine, B. T. 2003, ApJ, 598, 1017
Drake, A. J., Djorgovski, S. G., Prieto, J. L., et al. 2010, ApJL, 718, L127
Drlica-Wagner, A., Carlin, J. L., Nidever, D. L., et al. 2021, ApJS, 256, 2
Fitzpatrick, E. L., Massa, D., Gordon, K. D., Bohlin, R., & Clayton, G. C. 2019, ApJ, 886, 108
Flewelling, H. A., Magnier, E. A., Chambers, K. C., et al. 2020, ApJS, 251, 7
Gal-Yam, A. 2019, ApJ, 882, 102
Gal-Yam, A., Mazzali, P., Ofek, E. O., et al. 2009, Natur, 462, 624
Gehrels, N., Chincarini, G., Giommi, P., et al. 2004, ApJ, 611, 1005
Gomez, S., Nicholl, M., Berger, E., et al. 2024, MNRAS, 535, 471
Gordon, K. D., Cartledge, S., & Clayton, G. C. 2009, ApJ, 705, 1320
Gordon, K. D., Clayton, G. C., Decleir, M., et al. 2023, ApJ, 950, 86
Gordon, K. D., Misselt, K. A., Bouwman, J., et al. 2021, ApJ, 916, 33
Guillochon, J., Nicholl, M., Villar, V. A., et al. 2018, ApJS, 236, 6
Güver, T., & Özel, F. 2009, MNRAS, 400, 2050
Howell, D. A., Kasen, D., Lidman, C., et al. 2013, ApJ, 779, 98
Inserra, C., Smartt, S. J., Jerkstrand, A., et al. 2013, ApJ, 770, 128
Kangas, T., Blagorodnova, N., Mattila, S., et al. 2017, MNRAS, 469, 1246
Kasen, D., & Bildsten, L. 2010, ApJ, 717, 245
Kennicutt, R. C., Jr 1998, ARA&A, 36, 189
Könyves-Tóth, R. 2022, ApJ, 940, 69
Könyves-Tóth, R., & Seli, B. 2023, ApJ, 954, 44
Leloudas, G., Schulze, S., Krühler, T., et al. 2015, MNRAS, 449, 917
Lin, W., Wang, X., Yan, L., et al. 2023, NatAs, 7, 779
Lunnan, R., Chornock, R., Berger, E., et al. 2014, ApJ, 787, 138
Magnier, E. A., Chambers, K. C., Flewelling, H. A., et al. 2020, ApJS, 251, 3
Masci, F. J., Laher, R. R., Rusholme, B., et al. 2019, PASP, 131, 018003
Mazzali, P. A., Sullivan, M., Pian, E., Greiner, J., & Kann, D. A. 2016, MNRAS, 458, 3455
McCully, C., Turner, M., Volgenau, N., et al. 2018, LCOGT/banzai: Initial Release, v0.9.4,
Nicholl, M. 2018, RNAAS, 2, 230
Nicholl, M., Berger, E., Margutti, R., et al. 2017a, ApJL, 845, L8
Nicholl, M., Berger, E., Margutti, R., et al. 2017b, ApJL, 835, L8
Nicholl, M., Guillochon, J., & Berger, E. 2017c, ApJ, 850, 55
Nicholl, M., Smartt, S. J., Jerkstrand, A., et al. 2015, MNRAS, 452, 3869
Nicholl, M., Srivastav, S., Fulton, M. D., et al. 2023, ApJL, 954, L28
Oke, J. B., Cohen, J. G., Carr, M., et al. 1995, PASP, 107, 375
Onken, C. A., Wolf, C., Bessell, M. S., et al. 2024, PASA, 41, e061
Osterbrock, D. E., & Ferland, G. J. 2006, Astrophysics of Gaseous Nebulae and Active Galactic Nuclei (Univ. Science Books)
Pan, Y. C., Foley, R. J., Smith, M., et al. 2017, MNRAS, 470, 4241
Perley, D. A., Quimby, R. M., Yan, L., et al. 2016, ApJ, 830, 13
Poole, T. S., Breeveld, A. A., Page, M. J., et al. 2008, MNRAS, 383, 627
Poznanski, D., Prochaska, J. X., & Bloom, J. S. 2012, MNRAS, 426, 1465
Prochaska, J., Hennawi, J., Westfall, K., et al. 2020, JOSS, 5, 2308
Quimby, R. M., De Cia, A., Gal-Yam, A., et al. 2018, ApJ, 855, 2
Quimby, R. M., Kulkarni, S. R., Kasliwal, M. M., et al. 2011, Natur, 474, 487
Ridley, E. J., Nicholl, M., Ward, C. A., et al. 2024, MNRAS, 531, 1905
Rodrigo, C., Cruz, P., Aguilar, J. F., et al. 2024, A&A, 689, A93
Rodrigo, C., & Solano, E. 2020, in XIV.0 Scientific Meeting (virtual) of the Spanish Astronomical Society, 182
Rodrigo, C., Solano, E., & Bayo, A. 2012, SVO Filter Profile Service Version 1.0 Working Draft 15 October 2012, IVOA
Roming, P. W. A., Kennedy, T. E., Mason, K. O., et al. 2005, SSRv, 120, 95
Saito, S., Tanaka, M., Mazzali, P. A., Hachinger, S., & Hotokezaka, K. 2024, ApJ, 967, 13
Sana, H., de Mink, S. E., de Koter, A., et al. 2012, Sci, 337, 444
Schlafly, E. F., & Finkbeiner, D. P. 2011, ApJ, 737, 103
Schulze, S., Krühler, T., Leloudas, G., et al. 2018, MNRAS, 473, 1258
Shingles, L., Smith, K. W., Young, D. R., et al. 2021, TNSAN, 7, 1
Smartt, S. J., Valenti, S., Fraser, M., et al. 2015, A&A, 579, A40
Smith, K. W., Smartt, S. J., Young, D. R., et al. 2020, PASP, 132, 085002
Smith, M., Sullivan, M., Nichol, R. C., et al. 2018, ApJ, 854, 37
Smith, N., Li, W., Foley, R. J., et al. 2007, ApJ, 666, 1116
Steidel, C. C., Shapley, A. E., Pettini, M., et al. 2004, ApJ, 604, 534
Suzuki, A., Nicholl, M., Moriya, T. J., & Takiwaki, T. 2021, ApJ, 908, 99
Tonry, J. L., Denneau, L., Heinze, A. N., et al. 2018, PASP, 130, 064505
Villar, V. A., Nicholl, M., & Berger, E. 2018, ApJ, 869, 166
Vreeswijk, P. M., Savaglio, S., Gal-Yam, A., et al. 2014, ApJ, 797, 24
Xiang, D., Rui, L., Wang, X., et al. 2017, Transient Name Server Classification Report, 2017-599, 1
Yan, L., Perley, D. A., De Cia, A., et al. 2018, ApJ, 858, 91
Yan, L., Quimby, R., Gal-Yam, A., et al. 2017, ApJ, 840, 57
Young, D. R., & Landoni, M. 2023, The SOXS data-reduction pipeline, v0.8.0,
Zhu, J., Jiang, N., Dong, S., et al. 2023, ApJ, 949, 23